# A Kriged Compressive Sensing Approach to Reconstruct Acoustic Fields From Measurements Collected by Underwater Vehicles

Jie Sun, Member, IEEE, Shijie Liu, Member, IEEE, Fumin Zhang, Senior Member, IEEE, Aijun Song, Member, IEEE, Jiancheng Yu, and Aiqun Zhang

Abstract—This article presents a kriged compressive sensing (KCS) approach to reconstruct acoustic fields using measurements collected by underwater mobile sensing platforms. The KCS approach has two steps. First, initial estimates are obtained from a kriging method by leveraging spatial statistical correlation properties of the acoustic fields. Second, selected initial estimates, treated as virtual samples, are combined with the measurements to perform field reconstruction through compressive sensing. To differentiate the fidelity between real measurements and virtual samples, we use the kriging variance to determine weight coefficients for the virtual samples estimated from kriging. Simulation results show that the proposed KCS approach can improve the reconstruction performance, in terms of the peak signal-to-noise ratio and structural similarity metrics. The KCS performance has been validated based on the acoustic intensity measurements collected by an autonomous underwater vehicle in a lake. The KCS methods have also been applied to process the ambient sound level measurements collected by an underwater glider in the South China Sea. The proposed KCS method leads to better performance than either the compressive sensing or the kriging method alone.

*Index Terms*—Acoustic field reconstruction, compressive sensing (CS), kriging interpolation, underwater mobile platforms.

Manuscript received September 9, 2019; revised December 31, 2019; accepted February 10, 2020. This work was supported in part by the National Natural Science Foundation of China under Grant 61673370 and Grant U1709202, in part by the National Key Research and Development Project under Grant 2016YFC0301201, in part by the State Key Laboratory of Robotics at Shenyang Institute of Automation under Grant 2020-Z06 and Grant 2014-Z02, and in part by the U.S. National Science Foundation under Grants CNS-1828678 and S&AS-1849228. This article was presented in part at the 13th ACM International Conference on Underwater Networks & Systems (WUWNet'18), Dec. 3–5, 2018, Shenzhen, China. (Corresponding author: Aijun Song.)

## Associate Editor: J. Potter.

Jie Sun and Shijie Liu are with the State Key Laboratory of Robotics, Shenyang Institute of Automation, Chinese Academy of Sciences, Shenyang 110016, China, with the Institutes for Robotics and Intelligent Manufacturing, Chinese Academy of Sciences, Shenyang 110169, China, and also with the University of Chinese Academy of Sciences, Beijing 100049, China (e-mail: sunjie@sia.cn; liushijie@sia.cn).

Fumin Zhang is with the School of Electrical and Computer Engineering, Georgia Institute of Technology, Atlanta, GA 30332 USA (e-mail: fumin@gatech.edu).

Aijun Song is with the Department of Electrical Engineering, University of Alabama, Tuscaloosa, AL 35487 USA (e-mail: song@eng.ua.edu).

Jiancheng Yu and Aiqun Zhang are with the State Key Laboratory of Robotics, Shenyang Institute of Automation, Chinese Academy of Sciences, Shenyang 110016, China, and also with the Institutes for Robotics and Intelligent Manufacturing, Chinese Academy of Sciences, Shenyang 110169, China (e-mail: yjc@sia.cn; zaq@sia.cn).

Digital Object Identifier 10.1109/JOE.2020.2974270

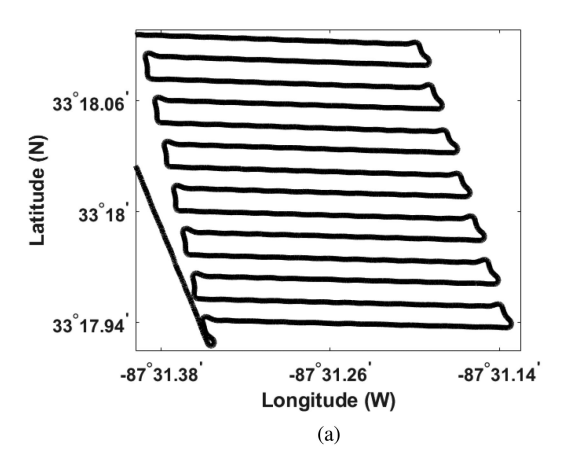
#### I. INTRODUCTION

OBILE sensing platforms, including AUVs and underwater gliders, can host hydrophones to collect acoustic measurements [1]–[5]. The sampling patterns of these mobile sensing platforms are formed by continuous trajectories that spread over a sampling area. Due to the kinematic constraints, these trajectories may not be evenly distributed over space. For example, AUVs usually travel along continuous comb-shaped paths in a sampling region [see Fig. 1(a)], whereas underwater gliders move along a sawtooth trajectory in the vertical plane [see Fig. 1(b)]. Considering the complex nature of the acoustic fields, the sampling performed by these mobile platforms is sparse in the vast sampling domain. Here, we focus on developing compressive sensing (CS) methods to reconstruct the acoustic fields based on the sparse trajectory-based measurements collected by underwater mobile platforms.

Geostatistical kriging [6] leverages spatial correlation structures to produce an interpolated mean field and the field of spatial covariance [7]–[9]. When estimating a spatial field from measurements, kriging achieves the least mean-square estimates of the underlying spatial data field [10]. Kriging techniques have been applied to construct spatial maps from data collected by marine robots [11], [12]. However, the ordinary kriging or other conventional approaches may cause the effect of oversmearing in estimates [13]–[15] where spatial patterns are weakened or removed. Spatial distributions of underwater acoustic characteristics are anisotropic due to the complicated water column property and dynamic boundary conditions [16], [17]. This article considers two types of acoustic fields, the field of transmission loss (TL) from an acoustic source and the ambient noise field. TL is a crucial parameter to acoustic systems in an underwater environment [18], [19]. Mapping ambient noise fields may support sonar operations and target detection [20], [21]. Both types of spatial acoustic fields share certain common anisotropy properties and spatial patterns that can be exploited by CS techniques [22], [23].

If spatial patterns are coherent and consistent in the acoustic fields, CS may work well with undersampled data [24]. The CS principle asserts that any sparse signal can be perfectly recovered from undersampled measurements if the sensing matrix satisfies the restricted isometry property (RIP) [22]. It is known that the RIP is usually satisfied if the measurements are taken at random

0364-9059 © 2020 IEEE. Personal use is permitted, but republication/redistribution requires IEEE permission. See https://www.ieee.org/publications/rights/index.html for more information.



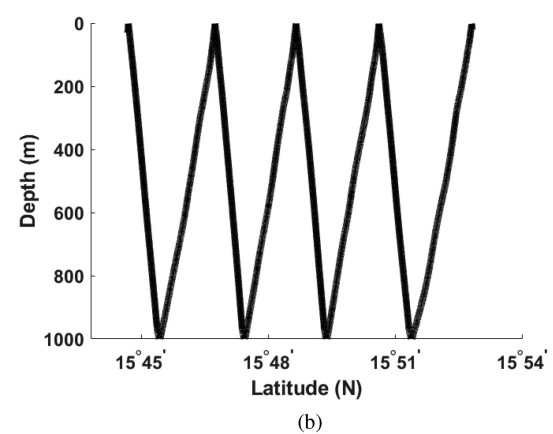


Fig. 1. Underwater vehicle trajectories. (a) Comb-shaped path of an AUV in the horizontal plane at Lake Tuscaloosa, AL, USA, on November 5, 2017. (b) Sawtooth trajectory of an underwater glider in the vertical plane in the South China Sea on August 28, 2018.

spatial locations [25]–[27]. However, due to the trajectory-based sampling from the mobile sensing platforms, the measurement locations are often not randomly distributed. Hence, the RIP required for faithful reconstruction may not be satisfied.

To improve the performance of construction algorithms, we here apply the concept of virtual samples to address the extremely low sampling rate from the vehicle trajectories. Virtual samples are created from the current set of examples incorporating prior knowledge [28]. Many methods have been developed to produce virtual samples to supplement the original measurements in image processing and supervised learning [29]–[32]. Virtual samples have also been used to improve the performance of CS. Interpolated CS (iCS) methods [33], [34] have been developed for magnetic resonance imaging and seismic imaging. The iCS methods produce interpolated samples based on Lagrangian polynomials [34] or interslice correlations [33].

We propose a kriged CS (KCS) method to reconstruct acoustic fields in the underwater environment. Our novel contributions are described below. A two-stage interpolation strategy, first kriging and then CS, has been proposed to reconstruct underwater acoustic fields based on measurements obtained from kinetically constrained sampling trajectories. The kriging method generates some virtual samples from physical measurements. Then, the CS techniques are applied to generate enhanced reconstruction of the acoustic fields. During the reconstruction using CS, the virtual samples are distinguished from the field measurements by introducing different weights for the samples. The weights are selected to be functions of the spatial variance in the data. Different from the iCS methods [33], [34], our method generates virtual samples directly in the spatial domain using kriging.

The kriging and CS combination offers multiple benefits. First, by adding the virtual samples, we introduce the randomness to the sensing matrix. This strategy improves the probability that the sensing matrix satisfies the RIP. Second, the kriging estimation variances are naturally used to compute weights of the virtual samples. Third, with enough samples, the CS strategy is able to exploit coherent structures in the acoustic fields. We show that the KCS method leads to better reconstruction of

acoustic fields than kriging or CS alone for both the ambient noise field and TL field from an active source. Two data sets are used to validate the KCS algorithm. One contains the acoustic data collected by an AUV in Lake Tuscaloosa in Alabama. The other contains ocean ambient noise data collected by a Sea-Wing underwater glider [35] during an experiment conducted in the South China Sea.

In the literature, there exist some efforts to investigate effective strategies for underwater sensing and exploration under the kinematic constraints. The related research issues were framed as the so-called kinematically constrained sparse approximation [36], where both the kinematic trajectories and sampling costs were considered. The focus was often to develop sensing strategies under the various resource constraints [37]–[39], for example, communication limits and energy costs associated with the underwater platforms. The CS approach was often assumed to be the method of sparse reconstruction. Unlike these efforts, this article focuses on developing sparse reconstruction algorithms based on kinematically constrained measurements.

Mapping of wireless radio frequency channels with mobile platforms was investigated in the literature. In [40], a sparsity-aware cooperative spectrum sensing method was proposed. The kriged Kalman filtering (KKF) was developed to estimate channel gain maps, with the aid of channel modeling. Then, the spectrum sensing task was accomplished by solving a sparse regression problem. Our proposal algorithm is different from the KKF algorithm, which is not a sparse strategy.

Our preliminary approach appeared as a conference paper [41]. In this article, we give further theoretical analysis, enhance the KCS method, and present a comprehensive validation of the algorithm based on field measurements. Specifically, we analyze the RIP for the proposed KCS method, compare different weight definitions, and utilize a block-based CS algorithm to solve the proposed Lagrangian problem. Experimental data are used to validate the proposed algorithms.

The rest of this article is organized as follows. We review relevant results of CS for image construction extended to acoustic field construction in Section II. In Section III, we propose the KCS method and present its implementation details. We

also provide the RIP analysis. In Section IV, we compare the performance of the proposed KCS methods with other alternatives based on a simulated TL spatial field sampled by a fleet of underwater gliders. In Section V, we analyze experimental data, including horizontal TL data collected by an AUV in a local lake and ocean ambient noise data collected by a glider during an experiment conducted in the South China Sea. In Section VI, we present the conclusions.

## II. REVIEW OF CS FOR IMAGE CONSTRUCTION

The CS principle asserts that certain signals can be recovered from a small set of measurements where there are coherent patterns [42]. However, the signal reconstruction problem is usually an underdetermined inverse problem that needs to be solved by imposing regularization constraints. We review relevant results in image construction that can be extended to acoustic field construction.

## A. Sparsity

If an image is compressible, a proper basis or dictionary can be utilized to extract the sparse information from the image. Suppose that we want to recover an  $m \times n$  spatially distributed field  $\mathbf{F}$ . When  $\mathbf{F}$  is sparse in a certain transform domain, a columnized vector,  $\mathbf{f} \in R^N(N=m \times n)$ , in  $\mathbf{F}$ , can be represented as

$$\mathbf{f} = \Psi \mathbf{x} \tag{1}$$

where  $\Psi$  is the  $N \times S$  transform matrix and coefficients  $\mathbf{x} \in R^S$  are a K-sparse signal with only  $K \ll N$  nonzero elements. Note that S is the number of basis in  $\Psi$  and S > N.

Many sparse transforms  $\Psi$  are available, including the Fourier transform, the wavelet transform (WT), and the contourlet transform (CT). For natural images, discontinuity points are typically located along smooth curves. WTs can isolate the discontinuities at edge points by enforcing point singularities and isotropic features [43], but are inadequate in recovering the smoothness along the curves or contours. CTs proposed in [44] consist of a double filter bank structure, including a Laplacian pyramid (LP) that is used to capture point discontinuities and a directional filter bank to link point discontinuity into linear structure. CTs can be viewed as a superposition of a WT and a directional transform. Compared with WTs, CTs provide a flexible number of directions with each of the scales allowing to capture the properties of curves or contours of images in its respective direction.

## B. Incoherent Sampling

Based on a sampling matrix  $\Phi \in R^{M \times N}$  with  $M \ll N$ , the columnized spatial field  $\mathbf{f}$  can be directly sampled as follows:

$$\mathbf{y} = \Phi \mathbf{f} + \epsilon = \Phi \Psi \mathbf{x} + \epsilon = \mathbf{A} \mathbf{x} + \epsilon \tag{2}$$

where  $\mathbf{y} \in R^M$  is a low-dimensional observation,  $\epsilon \in R^M$  denotes measurement noises, and  $\mathbf{A} := \Phi \Psi$  is the sensing matrix. The matrix  $\mathbf{A}$  is also called the equivalent dictionary. It is asserted that any K-sparse  $\mathbf{x}$  could be perfectly recovered from  $\mathbf{y}$  if  $\mathbf{A}$  satisfies the RIP [22]. The K-restricted isometry constant

is the smallest  $0 < \delta_s < 1$  such that for all  $n \le K$ 

$$(1 - \delta_s) \|\mathbf{x}_n\|_2^2 < \|\mathbf{A}_n \mathbf{x}_n\|_2^2 < (1 + \delta_s) \|\mathbf{x}_n\|_2^2$$
 (3)

where  $\|\cdot\|_2$  stands for the L2 norm,  $\mathbf{A}_n$  is a matrix formed by n columns extracted from the equivalent dictionary  $\mathbf{A}$ , and  $\mathbf{x}_n$  are the sparse coefficients corresponding to the n columns. The condition in (3) is equivalent to requiring that the Grammian matrix  $\mathbf{G} := \tilde{\mathbf{A}}_n^T \tilde{\mathbf{A}}_n$  has all of its eigenvalues in  $[1 - \delta_s, 1 + \delta_s]$ , where  $\tilde{\mathbf{A}}_n$  is  $\mathbf{A}_n$  with all its columns normalized and  $\tilde{\mathbf{A}}_n^T$  denotes the transpose of  $\tilde{\mathbf{A}}_n$ . In other words, the RIP ensures that any subset of columns of  $\mathbf{A}$  are nearly orthogonal. Since the equivalent dictionary  $\mathbf{A}$  has more columns than rows, i.e.,  $M \ll S$ , the columns of  $\mathbf{A}$  cannot be exactly orthogonal.

To ensure the RIP of order K with a high probability, the number of measurements M should not be too small. In [45] and [46], it was proven that under certain conditions, for accurate recovery of the K-sparse signal  $\mathbf{x}$ , the minimum number of measurements M should be  $O(K \log(S/K))$ .

## C. Solving the Inverse Problem

The inverse problem is formulated to solve for the signal f under sparsity constraints. If the sensing matrix A satisfies the RIP, we can recover f by finding the K-sparse coefficients of x as a solution to the optimization problem

$$\min \|\hat{\mathbf{x}}\|_1 \text{ subject to } \|\mathbf{W}^{1/2}(\mathbf{y} - \mathbf{A}\hat{\mathbf{x}})\|_2^2 \leqslant \xi \tag{4}$$

where  $\hat{\mathbf{x}}$  is the vector of recovered coefficients,  $\|\cdot\|_1$  stands for the L1 norm, constant  $\xi$  is a design parameter related to the strength of noise  $\epsilon$ , and matrix **W** is a positive definite weighting matrix that will be elaborated in Section III. A variety of algorithms have been proposed to solve the optimization problem (4), mainly including convex-programming approaches, greedy algorithms, and iterative thresholding algorithms [47], [48]. For the sake of complexity, the block-based CS (BCS) method [49] is considered in this article. This method divides the entire acoustic field into blocks and does the reconstruction for each block successively or simultaneously. However, along with this advantage, BCS methods also introduce blocking artifacts. To remove blocking artifacts, a pointwise adaptive Wiener filter [50] is incorporated into the iterative recovery procedure. By incorporating a weighting matrix W, we develop a variant of the BCS algorithms as shown in Algorithm 1.

The solution of  $\mathbf{x}$  to the problem in (4) also needs to satisfy the sparsity requirement. Hard thresholding can be applied. By setting an appropriate threshold  $\tau^{(i)}$  at each iteration, the iterative estimate of  $\mathbf{x}$  could be formulated by

$$\hat{\mathbf{x}}^{(i+1)} = \begin{cases} \hat{\hat{\mathbf{x}}}^{(i)}, \text{ for } |\hat{\hat{\mathbf{x}}}^{(i)}| \ge \tau^{(i)} \\ 0, \text{ for } |\hat{\hat{\mathbf{x}}}^{(i)}| < \tau^{(i)} \end{cases}$$
(5)

where  $\hat{\hat{\mathbf{x}}}^{(i)}$  represents the initial estimate, which is not necessarily sparse, at the *i*th iteration.

The iterative algorithm uses the difference between the reconstructed fields before and after the thresholding step, that is

**Algorithm 1:** Block-based Compressive Sensing with Smoothing Weighted Landweber Iteration and Hard Thresholding Recovery (BCS-SWLT).

**Input:** measurement vector  $\mathbf{y}$ , sampling matrix  $\Phi$ , transform matrix  $\Psi$ , weight matrix  $\mathbf{W}$ , thresholding function *Thresholding*( $\mathbf{x}$ ), and error tolerance  $\delta$  for each block j do

```
Generate \mathbf{y}_j, \Phi_{Bj}, and \mathbf{W}_{Bj}
         Initialize i = 0, \mathbf{D}^{(0)} = 0, \mathbf{f}_{i}^{(0)} = \Phi_{Bi}^{T} \mathbf{y}_{i}
end
repeat
         \hat{\mathbf{f}}^{(i)} = Wiener(\mathbf{f}^{(i)})
         for each block j do
           \hat{\mathbf{f}}_{i}^{(i)} = \hat{\mathbf{f}}_{i}^{(i)} + \Phi_{Bj}^{T} \mathbf{W}_{Bj}^{1/2} (\mathbf{y}_{j} - \Phi_{Bj} \hat{\mathbf{f}}_{i}^{(i)})
          \hat{\hat{\mathbf{x}}}^{(i)} = \Psi^{-1}\hat{\hat{\mathbf{f}}}^{(i)}
         \hat{\mathbf{x}}^{(i+1)} = Thresholding(\hat{\hat{\mathbf{x}}}^{(i)})
         \mathbf{\hat{f}}^{(i+1)} = \mathbf{\Psi}\mathbf{\hat{x}}^{(i+1)}
           \hat{\hat{\mathbf{f}}}_{j}^{(i+1)} = \hat{\mathbf{f}}_{j}^{(i+1)} + \Phi_{Bj}^{T} \mathbf{W}_{Bj}^{1/2} (\mathbf{y}_{j} - \Phi_{Bj} \hat{\mathbf{f}}_{j}^{(i+1)}) 
         \mathbf{D}^{(i+1)} = \|\hat{\hat{\mathbf{f}}}^{(i+1)} - \hat{\hat{\mathbf{f}}}^{(i)}\|_{2}
         \mathbf{f}^{(i+1)} \leftarrow \hat{\hat{\mathbf{f}}}^{(i+1)}
         i \leftarrow i + 1
until |{\bf D}^{(i+1)} - {\bf D}^{(i)}| < \delta;
Output: recover \mathbf{f} = \mathbf{f}^{(i)}
```

 $\mathbf{D}^{(i+1)} = \|\hat{\mathbf{f}}^{(i+1)} - \hat{\mathbf{f}}^{(i)}\|_2$ , in the exit criterion. If the improvement of  $\mathbf{D}^{(i+1)}$ , defined as  $|\mathbf{D}^{(i+1)} - \mathbf{D}^{(i)}|$ , is smaller than a preset threshold  $\delta$ , the iterative process is terminated.

## D. Performance Metrics

Two relevant evaluation metrics from compressive imaging are adopted to measure the performance of spatial reconstruction algorithms, the peak signal-to-noise ratio (PSNR) [51] and the structural similarity (SSIM) [52] index.

1) PSNR: It estimates absolute errors of the reconstruction. It is defined as the ratio between the maximum possible signal power of the field and the power of corrupting noise that distorts it. The PSNR is derived from the root-mean-square error (RMSE) as follows:

$$PSNR = 20 \log_{10} \left( \frac{MAX_I}{RMSE(\mathbf{F}, \mathbf{F}_{rec})} \right)$$
 (6)

where  $\mathbf{F}_{rec} \in R^{m \times n}$  is the reconstructed 2-D spatial field,  $MAX_I$  is the maximum possible value of the field, and

$$RMSE = \sqrt{\frac{1}{m \times n} \sum_{i=1}^{m} \sum_{j=1}^{n} [\mathbf{F}(i,j) - \mathbf{F}_{rec}(i,j)]^{2}}.$$
(7)

2) SSIM Index: It is a perception-based model to measure the similarity between two images. As proven to be consistent with human eye perception, it is a combination of three comparison measurements between the original image  $\mathbf{F}$  and the reconstructed image  $\mathbf{F}_{rec}$ , including luminance (l), contrast (c),

and structure (s)

$$SSIM = l(\mathbf{F}, \mathbf{F}_{rec}) \times c(\mathbf{F}, \mathbf{F}_{rec}) \times s(\mathbf{F}, \mathbf{F}_{rec}). \tag{8}$$

The individual comparison functions are

$$l(\mathbf{F}, \mathbf{F}_{rec}) = \frac{2(\mu_{\mathbf{F}} \times \mu_{\mathbf{F}_{rec}}) + c_1}{\mu_{\mathbf{F}}^2 + \mu_{\mathbf{F}_{rec}}^2 + c_1}$$
(9)

$$c(\mathbf{F}, \mathbf{F}_{rec}) = \frac{2(\sigma_{\mathbf{F}} \times \sigma_{\mathbf{F}_{rec}}) + c_2}{\sigma_{\mathbf{F}}^2 + \sigma_{\mathbf{F}_{rec}}^2 + c_2}$$
(10)

$$s(\mathbf{F}, \mathbf{F}_{rec}) = \frac{\sigma_{\mathbf{F}, \mathbf{F}_{rec}} + c_3}{\sigma_{\mathbf{F}} \times \sigma_{\mathbf{F}_{rec}} + c_3}$$
(11)

where  $\mu_{\mathbf{F}}$  is the average of  $\mathbf{F}$ ,  $\mu_{\mathbf{F}_{\mathrm{rec}}}$  is the average of  $\mathbf{F}_{\mathrm{rec}}$ ,  $\sigma^2_{\mathbf{F}}$  is the variance of  $\mathbf{F}$ ,  $\sigma^2_{\mathbf{F}_{\mathrm{rec}}}$  is the variance of  $\mathbf{F}_{\mathrm{rec}}$ ,  $\sigma_{\mathbf{F},\mathbf{F}_{\mathrm{rec}}}$  is the covariance of  $\mathbf{F}$  and  $F_{\mathrm{rec}}$ , and  $F_{\mathrm{rec}}$ , and  $F_{\mathrm{rec}}$ , and  $F_{\mathrm{rec}}$  is the equation,  $F_{\mathrm{rec}}$  and  $F_{\mathrm{rec}}$  are two variables to stabilize the division with  $F_{\mathrm{rec}}$  as the dynamic range of the pixel values.

## E. Problem Setup

For the spatial sampling of acoustic fields, the sampling patterns of the underwater vehicles are formed by continuous trajectories. The sampling matrix  $\Phi$  is often not a random matrix, neither would the sensing matrix  $\mathbf{A}$ . Therefore, some subsets of columns of  $\mathbf{A}$  may be linearly dependent. Furthermore, the practical sampling rate cannot achieve a high level due to the vast sampling domain. Hence, it is quite challenging to ensure the RIP, which is a prerequisite to achieve a full construction of the K-sparse vector  $\mathbf{x}$  directly from the kinetically constrained measurements. We show that this problem can be addressed by our KCS method in Section III.

## III. KRIGED COMPRESSIVE SENSING

To improve the probability that the sensing matrix  $\mathbf{A}$  satisfies the RIP, the primary strategy is to increase the number of measurements M and simultaneously to decrease the coherence among different columns of  $\mathbf{A}$ . The ideal solution is to make the sensing matrix  $\mathbf{A}$  close to a random matrix. The proposed solution is to add virtual samples to the set of real measurements to increase the measurement sample size. The virtual samples are randomly selected estimates that are generated from the kriging interpolation.

## A. Kriging

The kriging methods calculate an estimate at a point of interest (POI) based on the statistical properties, e.g., mean and covariance, of the spatially distributed data. The spatial covariance is considered as a function of the relative distance between data points. Let  $h(p_i,p_j)$  be the distance between any two sampling locations  $p_i$  and  $p_j$ . For any particular distance value d, we define  $\mathcal{N}(d)$  to be the set of all i,j such that  $h(p_i,p_j)=d$ . The semivariogram values are first calculated from the measurements [53] as follows:

$$\gamma(d) = \frac{1}{2|\mathcal{N}(d)|} \sum_{i,j \in \mathcal{N}(d)} [y(p_i) - y(p_j)]^2$$
 (12)

where  $y(p_i)$  and  $y(p_j)$  are the measurements. The notation  $|\mathcal{N}(d)|$  refers to the number of paired data in the set  $\mathcal{N}(d)$ . The semivariogram  $\gamma(\cdot)$  is then interpolated for all distance values based on a selected kernel, such as exponential kernels or Gaussian kernels. The covariance function  $C_{i,j} := C(h(p_i, p_j))$  is obtained as  $C(h(p_i, p_j)) = C(0) - \gamma(h(p_i, p_j))$ , in which C(0) corresponds to the empirical autocorrelation calculated from the real measurements.

We use the ordinary kriging method to generate virtual measurements at POIs, based on the real measurements. Let  $p_0$  be a POI that is randomly selected as a virtual sampling point. To produce the interpolated value at  $p_0$ , we first find the correlation among  $p_0$  and any of the real sampling point  $p_i$ . By introducing the Lagrangian multiplier  $\nu$ , the weights  $\lambda_i$  for interpolation are obtained by the following equation:

$$\begin{bmatrix} 1 & C_{1,1} & \cdot & C_{1,M} \\ \vdots & & \vdots & & \\ 1 & C_{M,1} & \cdot & C_{M,M} \\ 0 & 1 & \cdot & 1 \end{bmatrix} \begin{bmatrix} \nu \\ \lambda_1 \\ \vdots \\ \lambda_M \end{bmatrix} = \begin{bmatrix} C_{1,0} \\ \vdots \\ C_{M,0} \\ 1 \end{bmatrix}.$$

The kriging estimate at  $p_0$  is calculated as

$$y(p_0) = \sum_{i=1}^{M} \lambda_i \times y(p_i). \tag{13}$$

The kriging variance for a virtual sample  $y(p_0)$  is obtained as

$$\sigma^{2}(p_{0}) = C(0) - \sum_{i=1}^{M} \lambda_{i} \times C(h(p_{i}, p_{0})) - \nu.$$
 (14)

## B. Solving CS Parameters

After obtaining the random virtual samples, we now have two sets of measurements, the collection of real measurements  $\mathbf{y}_{\mathrm{real}}$  and the collection of virtual measurements  $\mathbf{y}_{\mathrm{virtual}}$ . The virtual sampling points are only selected at the points with no real sampling values. The aggregated measurements can be organized into a column vector as

$$\mathbf{y} = [\mathbf{y}_{\text{real}}^T \ \mathbf{y}_{\text{virtual}}^T]^T. \tag{15}$$

Suppose the number of virtual samples is  $M_v$ , then the number of overall measurements is  $M_o=M+M_v$ . So, we can define the overall sampling rate as the sum of the real sampling rate and virtual sampling rate. The measurement equation follows (2) while both the sensing matrix  $\Phi$  and the measurement noise  $\epsilon$  are enlarged to include the virtual samples.

## C. RIP for Enlarged Equivalent Dictionary

The RIP requires that any subset of columns of the enlarged equivalent dictionary  $\tilde{\mathbf{A}}$  is nearly orthogonal. One way to achieve this is to make the Grammian matrix  $\mathbf{G} = \tilde{\mathbf{A}}^T \tilde{\mathbf{A}}$  as close to the identity matrix  $\mathbf{I}_S$  as possible. The off-diagonal elements in the Grammian matrix should be almost zero when the RIP is satisfied. If we express  $\tilde{\mathbf{A}} \in R^{M \times S}(M \ll S)$  as  $\tilde{\mathbf{A}} = [\tilde{\mathbf{a}}_1, \dots, \tilde{\mathbf{a}}_S]$ ,

an off-diagonal element of the Grammian matrix is

$$g_{ij} = \tilde{\mathbf{a}}_i^T \cdot \tilde{\mathbf{a}}_i \ (i \neq j, 1 \leq i, j \leq S). \tag{16}$$

Here, we adopt the averaged mutual coherence defined in [54] to measure the mean square error for the nonzero off-diagonal elements

$$\mu_{\mathbf{A}} := \frac{\sum_{i \neq j, 1 \le i, j \le S} g_{ij}^2}{S(S-1)}.$$
 (17)

Since  $\tilde{\mathbf{A}}$  has more columns than rows, i.e.,  $S\gg M$ , the rank of matrix  $\tilde{\mathbf{A}}$  cannot exceed M. Suppose  $\mathrm{rank}(\tilde{\mathbf{A}})=Q, (Q\leq M)$ , then Q of S columns are the orthonormal basis. Without loss of generality, we assume that the first Q vectors of  $\tilde{\mathbf{A}}$  correspond to the orthonormal basis. We can calculate the number of nonzero off-diagonal elements in the Grammian matrix  $\mathbf{G}$ , i.e., the L0 norm,  $\|\cdot\|_0$  of nonzero off-diagonal elements. Considering two cases, for  $i\in[1,Q]$ 

$$\|\{g_{ij}|i\in[1,Q],j\in[1,S],i\neq j\}\|_0=Q(S-Q)$$

and for  $i \in [Q+1, S]$ 

$$\|\{g_{ij}|i\in[Q+1,S],j\in[1,S],i\neq j\}\|_0=(S-Q)(S-1).$$

Hence

$$\|\{g_{ij}|i,j\in[1,S],i\neq j\}\|_{0} = Q(S-Q) + (S-Q)(S-1)$$

$$= S^{2} - S - Q(Q-1).$$
(18)

Since

$$\frac{\partial \|\{g_{ij}|i,j\in[1,S], i\neq j\}\|_0}{\partial Q} = -2Q+1 < 0$$

the function in (18) is monotonically decreasing, when  $Q \geq 1$ .

For the KCS strategy, since the added virtual samples are randomly selected, the rank of matrix  $\tilde{\bf A}$  increases from Q to  $Q+M_v$ . According to (18), there are less nonzero off-diagonal elements in the Grammian matrix  ${\bf G}$  than the case with no virtual measurements. Furthermore, the values of nonzero off-diagonal elements in the Grammian matrix  ${\bf G}$  do not increase because random items have no coherence. Therefore, according to (17), the mutual coherence measure is reduced by the addition of virtual measurements, i.e.,

$$\mu_{\mathbf{A}}|_{\mathrm{KCS}} < \mu_{\mathbf{A}}|_{\mathrm{CS}}.$$

Therefore, the expanded sensing matrix A is more likely to be orthogonal and to satisfy the RIP of order K.

# D. Weights of Virtual Measurements

In the KCS framework, we distinguish the fidelity between real and virtual measurements by using the diagonal weighting matrix W. The diagonal elements of W are specified as

$$\omega_i = \begin{cases} 1, & \text{for } i = 1, \dots, M \\ \eta_i, & \text{for } i = M + 1, \dots, M + M_v. \end{cases}$$
 (19)

Specifically, the weights corresponding to real samples are all set to 1. The weights corresponding to virtual samples are set to  $\eta_i \in [0, 1]$ . The weights reflect the fact that the virtual samples

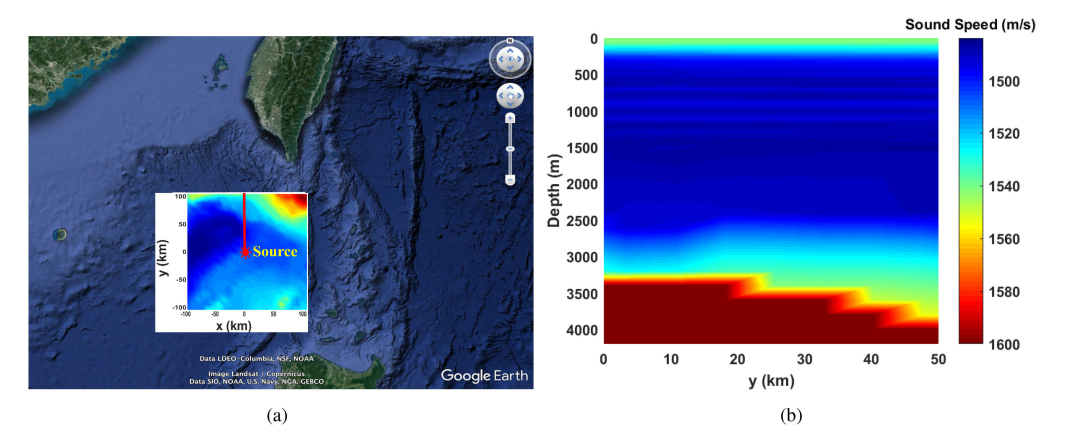


Fig. 2. Simulation environment. (a) Selected simulation site in the South China Sea near the Luzon Strait. An acoustic source, marked as "Source," is deployed at the center of this region with coordinates (20°18′12.29″ N, 119°57′7.28″ E). The source point is set as the origin for display and analysis. The vertical line in the center inset shows the projection of the vertical plane selected for field reconstruction. (b) Sound speed distribution for the selected 2-D plane.

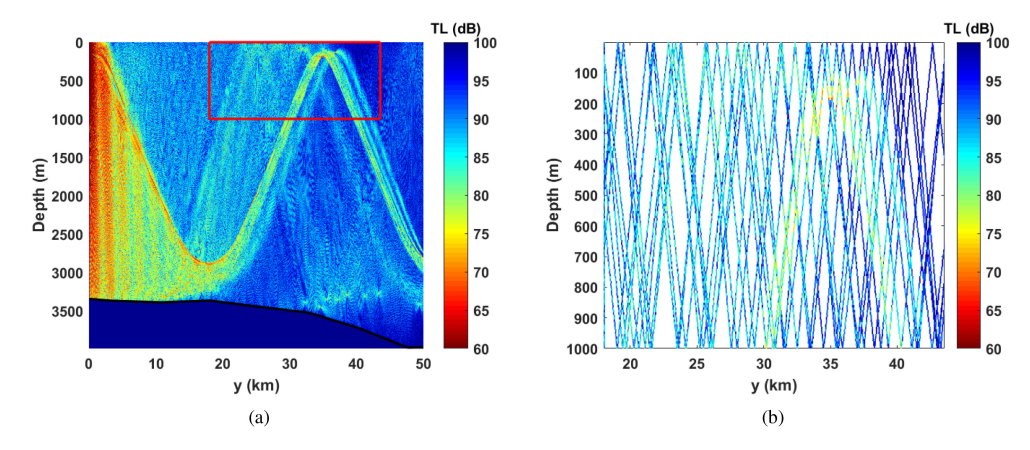


Fig. 3. Simulated TL field and sampling. (a) Simulated TL spatial field within the vertical plane in Fig. 2(b). The marked rectangular area is selected to conduct further reconstruction. (b) TL measurements sampled by underwater gliders along sawtooth trajectories.

 $\mathbf{y}_{\text{virtual}}$  have nonzero estimation errors. Virtual samples with larger estimation errors are assigned with smaller weights.

Among all the kriging estimates, we can find the minimum estimation variance  $\sigma_{\min}^2$  from (14). By referring to the weight defined when considering the frequency domain sensitivity for the visual entropy [55], [56] and applying the noisy measurements in particle physics [42], one may choose the weights as

$$\eta_{I,i} = \sigma_{\min}^2 / \sigma_i^2. \tag{20}$$

In our previous work [41], we gave another choice of weights

$$\eta_{II,i} = \left(1 - \frac{\sigma_i}{\sigma_{\text{max}}}\right)^2 \tag{21}$$

where  $\sigma_{\rm max}$  is the square root of the maximum kriging estimation variance. Note that the two types of weights in (20) and (21) are not equivalent in performance. As shown later, the choice of weighting methods depends on applications. Both methods can be tried and the one with better performance can be selected.

## IV. SIMULATION STUDY

We carry out computer simulations based on the environmental data in the South China Sea near the Luzon Strait, shown in Fig. 2(a). The bathymetry in this region is obtained from geospatial data from the NOAA website [57]. The sound speed distribution in this region is calculated from the hydrological data acquired from POM South China Sea 1/15° analysis provided by the South China Sea Institute of Oceanology, Guangzhou, China [58]. The acoustic TL field at this site is generated using the toolbox Bellhop 3D, which is published at the Ocean Acoustics Library [59].

From the generated 3-D acoustic field, we extract a 2-D vertical slice whose location is indicated by the vertical line in Fig. 2(a). The sound speed distribution over this vertical plane is shown in Fig. 2(b). Fig. 3(a) is the extracted 2-D TL spatial field.

In the simulations, a fleet of underwater gliders is deployed into a sampling area of Depth :  $1 \text{ km} \times \text{y}$ : 25.55 km, as marked by a rectangle in Fig. 3(a). Simulated acoustic intensity within this area is the ground truth for acoustic field reconstruction.

We then simulate that multiple gliders navigate along sawtooth trajectories. Based on the simulated measurements collected by the gliders, different reconstruction algorithms are used to construct the acoustic field in the sampling region [marked in a rectangular box in Fig. 3(a)]. Through comparison with the ground truth, we evaluate the performance of the proposed KCS

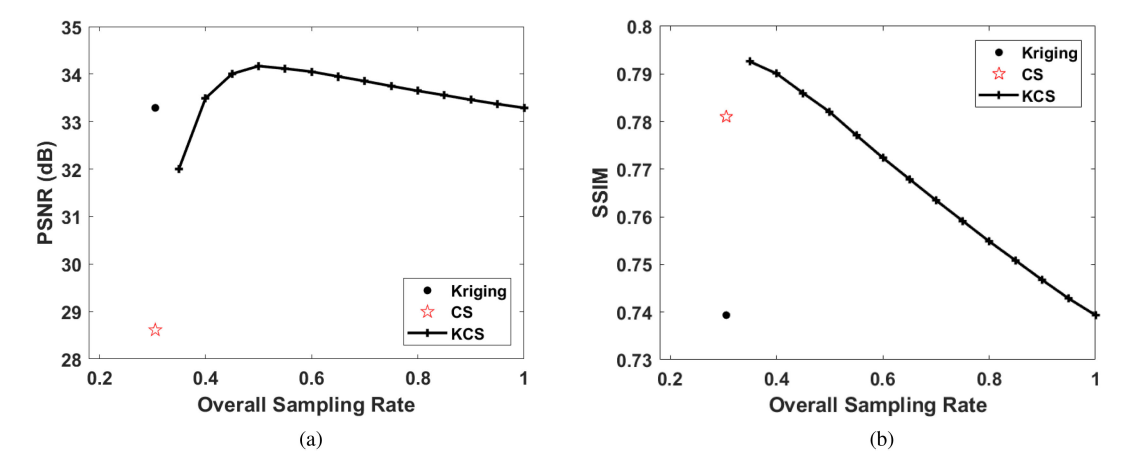


Fig. 4. Unweighted KCS reconstruction performance under different overall sampling rates. (a) PSNR and (b) SSIM index. The CS and kriging performances are shown for comparison.

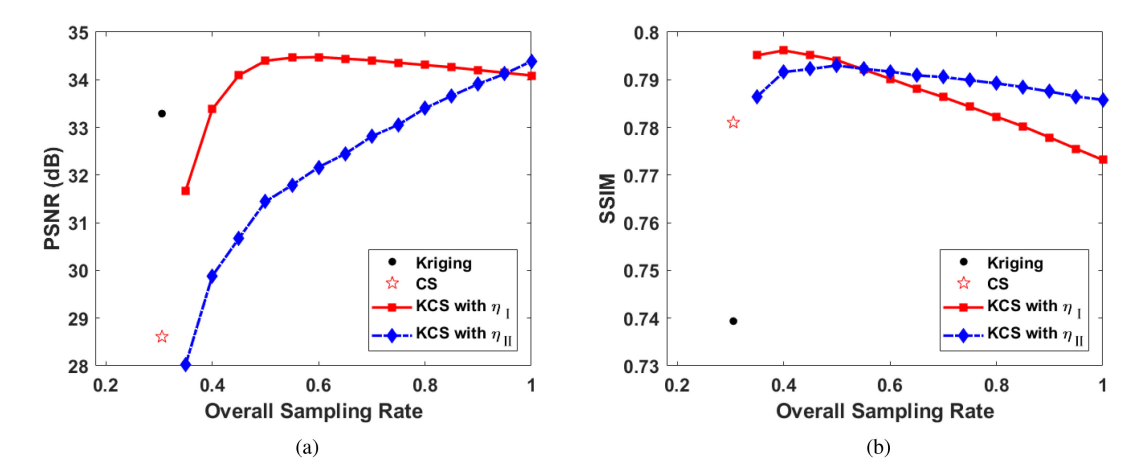


Fig. 5. Reconstruction performance of different weighted KCS algorithms under different overall sampling rates. (a) PSNR metric and (b) SSIM indexes. The CS and kriging performances are shown for comparison.

algorithms. We use the exponential kernel for all the kriging procedures in the simulations.

## A. Performance of Unweighted KCS

Eight gliders are simulated. Each of them is equipped with a hydrophone. The samples along glider trajectories are shown in Fig. 3(b). By setting the spatial resolution to about Depth :  $8 \text{ m} \times \text{y}$ : 50 m, the discretized dimension of the selected area is  $128 \times 512$ . After arranging the measurements into pixels, the corresponding real sampling rate is 30.54%.

Based on the simulated trajectory-based measurements, we compare the performance of three field reconstruction methods. The first method is CS on the real samples only (labeled as CS in Fig. 4). The second method is kriging-only (labeled as kriging in Fig. 4). The third method is KCS, with all weights of samples set to 1 (labeled as KCS in Fig. 4). We call this case unweighted KCS, since it does not distinguish the real samples from the virtual samples.

Each data point plotted in Fig. 4 represents the averaged performance metric over multiple trials. For the KCS method, we plot the metric values as the overall sampling rate increases.

In Fig. 4(a), we can observe that increasing the number of virtual samples accounts for the initial improvement in the PSNR metric. The added virtual samples lead to a decrease in the PSNR metric when the overall sample rate is higher than 50% for this case. In Fig. 4(b), the SSIM index value decreases as more virtual samples are introduced. This is because the kriging method has the effect to smear the spatial pattern. We can also observe that kriging alone performs well at low sampling rates when the PSNR metric is used for evaluation. However, kriging alone does not generate a comparable high SSIM index. This can be explained by the smearing effect of kriging. For both metrics, when the overall sampling rate is 100%, the performance of the KCS algorithm is identical to that of the kriging alone. This indicates that weighting the virtual samples may be necessary to further improve the performance of KCS.

## B. Comparison Among KCS With Different Types of Weights

Using the same simulated case in Fig. 3(b), we explore the performances of weighted KCS algorithms with different weighting functions under different virtual sampling rates, see Fig. 5. The CS-only and kriging-only performance are also

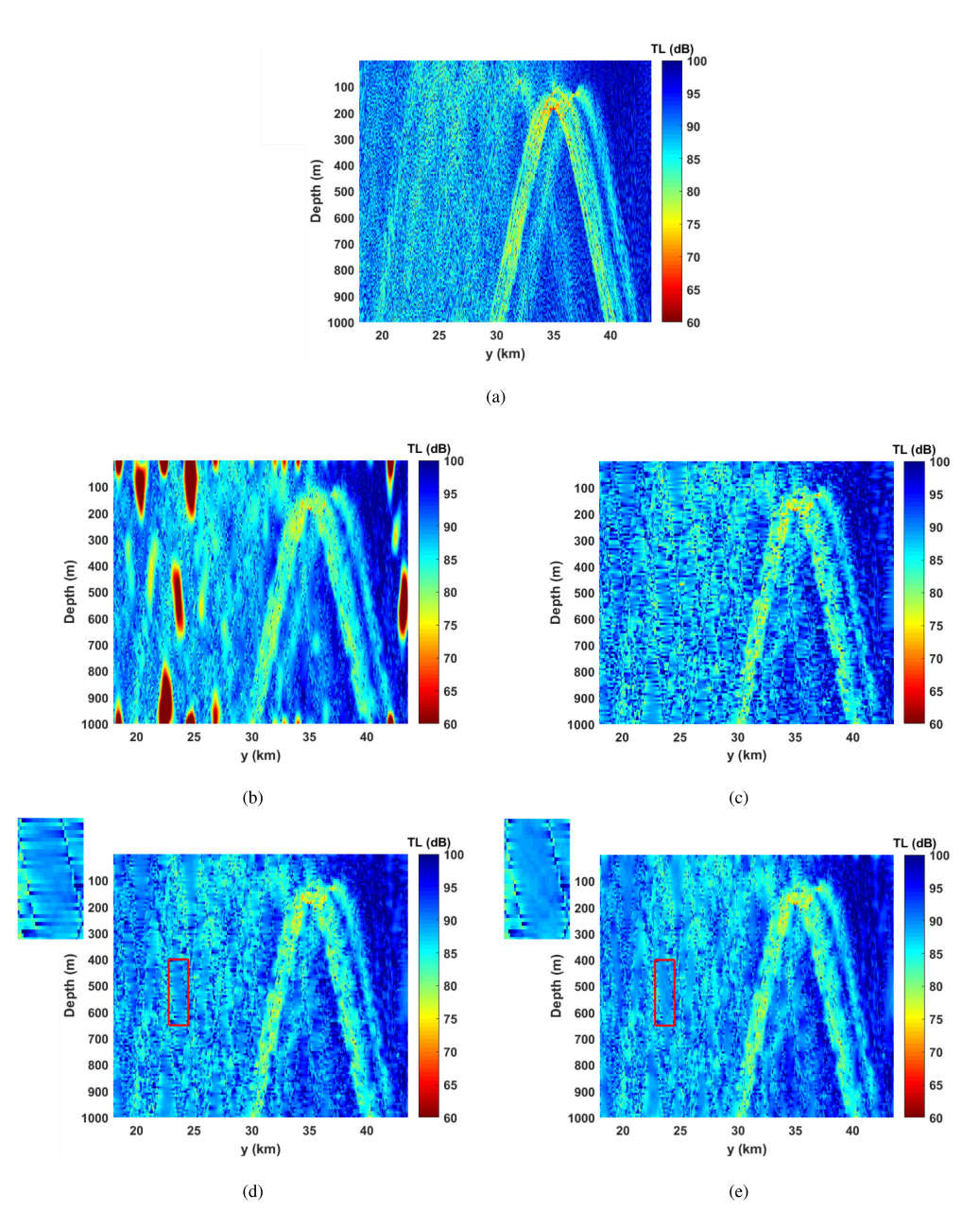


Fig. 6. Original field image and its reconstructions. (a) Original field image. Fields constructed from (b) the CS method, (c) the kriging method, (d) weighted KCS with  $\eta_I$ , and (e) weighted KCS with  $\eta_{II}$ . The marked rectangular areas in (d) and (e) are enlarged.

shown for comparison. For the PSNR metric, the performance of weighted KCS with  $\eta_{II}$  increases with the overall sampling rate. The performance of weighted KCS with  $\eta_{I}$  increases first and then decreases. This behavior is similar to that of the unweighted KCS method. When the overall sampling rate reaches to 100%, the PSNR value corresponding to weighted KCS with  $\eta_{I}$  decreases to 34.09 dB, whereas the PSNR value corresponding to unweighted KCS decreases to 33.29 dB. Hence, we see that performances of weighted KCS with both weighting functions are improved. For the SSIM metric, weighted KCS with both weighting functions lead to a decreasing trend in performance when more virtual samples are introduced. However, the rates of decline are significantly reduced due to weighting. The SSIM curve for weighted KCS with  $\eta_{II}$  has the lowest rate of decline.

At the 100% overall sampling rate, the weighted KCS approach outperforms kriging alone.

Fig. 6 plots the reconstructed images based on different algorithms. Note that Fig. 6(a) shows the original field. Just based on real samples, we generate a CS-reconstructed field in Fig. 6(b) and kriging-estimated field in Fig. 6(c). The images in Fig. 6(d) and (e) are reconstructed by the weighted KCS with weights defined as  $\eta_I$  and  $\eta_{II}$ , respectively. For all the weighted KCS algorithms, the overall sampling rate is set to 100%. The performance metrics are given in Table I. For this case, the KCS algorithm with the weight set to  $\eta_{II}$  performs the best.

The above-mentioned comparison is repeated for different numbers of sampling gliders. We observe similar performance trends that favor the weighted KCS method.

TABLE I Performance Metrics of Reconstructed Fields Under Real Sampling Rate 30.54% and Overall Sampling Rate 100%

	CS	Kriging	weighted KCS	
			$\eta_I$	$\eta_{II}$
PSNR	28.61	33.29	34.09	34.39
SSIM	0.781	0.739	0.773	0.786

TABLE II CONTOURLET COEFFICIENT COMPARISON AMONG DIFFERENT RECONSTRUCTED IMAGES

	CS	Kriging	weighted KCS	
	CS		$\eta_I$	$\eta_{II}$
Nonzero Rate	5.93%	18.53%	9.67%	6.81%
RMSE	6.91	1.94	1.69	1.61

## C. Explanation of Results

The introduction of virtual samples that are initially obtained by the kriging method tends to remove high-frequency spatial variations and thus weakens spatial patterns. By adding virtual samples, the KCS approach achieves improved reconstruction over the CS because the sampling matrix has a higher probability to satisfy the RIP.

This explanation is justified by Table II, where the first row lists the rate of nonzero coefficients of the contourlets  $\hat{\mathbf{x}}$ . The second row lists the RMSE value of the coefficients compared with the values of these coefficients computed based on the ground truth shown in Fig. 6(a). The rate of nonzero coefficients is defined as the number of nonzero coefficients  $\|\hat{\mathbf{x}}\|_0$  divided by the total number of image pixels N. Although the rate corresponding to the CS method is small, the estimated coefficients are not consistent with the true coefficients. This causes a large RMSE value as shown in Table II. This illustrates that the CS method may miscalculate the coefficients.

Fig. 7 shows the reconstructed sparse coefficients of the CS and the KCS methods compared with real coefficients in the lowpass subband, i.e.,  $(\hat{\mathbf{x}} - \mathbf{x})|_{LP}$ . Noted in Table II, the rate of nonzero coefficients for kriging-only is the largest, which illustrates that kriging smears the spatial pattern. By adding weighted virtual samples and combining kriging with CS, we can achieve a small rate of nonzero coefficients, as well as a low RMSE in the coefficients.

## V. EXPERIMENTAL DATA AND ANALYSIS

In this section, we demonstrate the effectiveness of the weighted KCS method in two field experiments. A Sea-Wing underwater glider was deployed in the South China Sea to measure the ambient noise level in the ocean. We constructed the noise field in the vertical plane that encompasses the glider trajectories. An EcoMapper AUV equipped with a hydrophone was deployed in Lake Tuscaloosa, Alabama, USA, to measure the horizontal field of acoustic TL. We constructed the TL field in the horizontal plane.

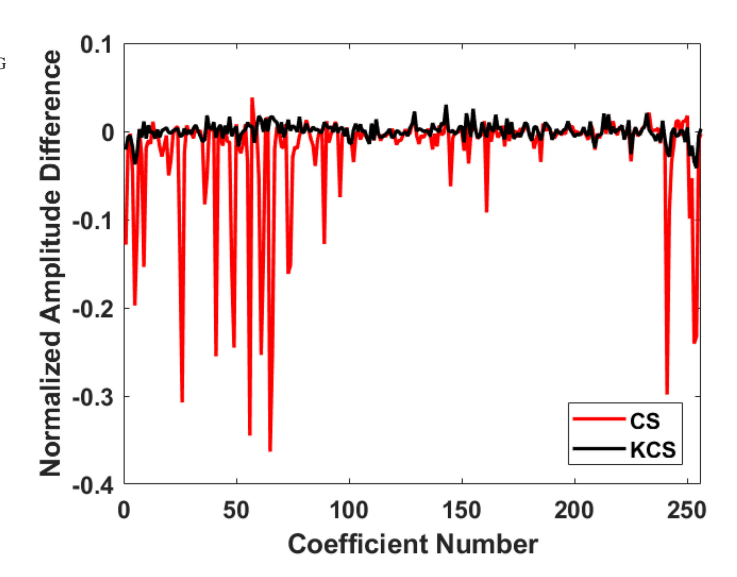


Fig. 7. Reconstructed sparse coefficients compared to real coefficients in the lowpass subband. The *x*-axis represents the coefficient number of the lowpass subband. The *y*-axis stands for the normalized amplitude difference between CS or KCS coefficients and the ground truth, respectively.

Different from simulations, the field experiments did not provide the ground truth to evaluate reconstruction performance. Hence, the SSIM metric cannot be used here. Instead, we used the tenfold cross-validation method to perform the reconstruction and then evaluated the performance based on data points that were not used for reconstruction. The real samples Y were randomly partitioned into ten sets of equal-sized subsamples  $\{Y_1, Y_2, \ldots, Y_{10}\}$ . At the  $i\text{th}(i=1,\ldots,10)$  trial of reconstruction, a single set of subsamples  $Y_i$  was retained as the validation data. The remaining nine subsample sets  $\{Y_1,\ldots,Y_{i-1},Y_{i+1},\ldots,Y_{10}\}$  were used for field reconstruction. For evaluation, we calculated the RMSE of the reconstructed image at the locations of validation data Location<sub>val</sub>. To show the comparison among different reconstruction methods, we converted the RMSE value to the PSNR as follows:

$$\text{PSNR}|_{\text{Location}_{\text{val}}} = 20 \log_{10} \left( \frac{\text{MAX}_I}{\text{RMSE}(\mathbf{f}, \mathbf{f}_{\text{rec}})|_{\text{Location}_{\text{val}}}} \right).$$

## A. Reconstruction of Ambient Noise Field

Fig. 8(a) shows the ambient sound level sampled along the glider trajectories in an experiment conducted in the South China Sea in August 2018. Although the glider has low self-noise, the noise from the oil pump working near the sea surface or the seafloor could severely contaminate the measurements. Hence, we selected an area avoiding the shallow and deep areas to apply the KCS for reconstruction.

The glider carried an onboard hydrophone. The sampling frequency of the hydrophone (developed by Institute of Acoustics, Chinese Academy of Sciences, Beijing, China) was set to 8 kHz. During the data processing, we focused on the ambient noises range between 200 Hz and 2 kHz. This frequency band included the shipping and wind noises while excluding the vehicle self-noise. After the bandpass filtering, the acoustic intensity was calculated by averaging the acoustic power of the

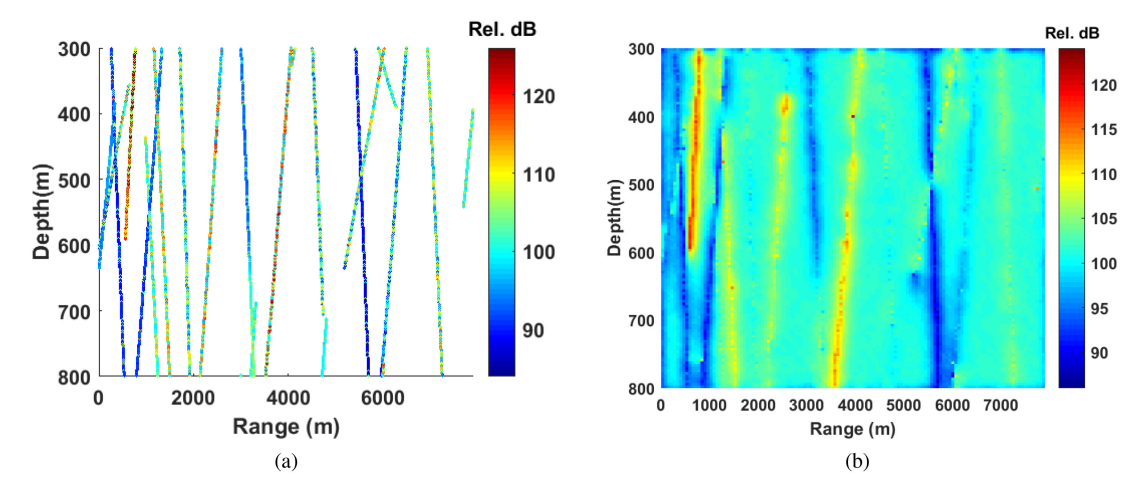


Fig. 8. Reconstruction by the weighted KCS with  $\eta_{II}$ . The real sampling rate was 11.66% and the overall sampling rate was 100%. (a) Ambient sound level sampled along the glider trajectories. (b) Reconstructed spatial field.

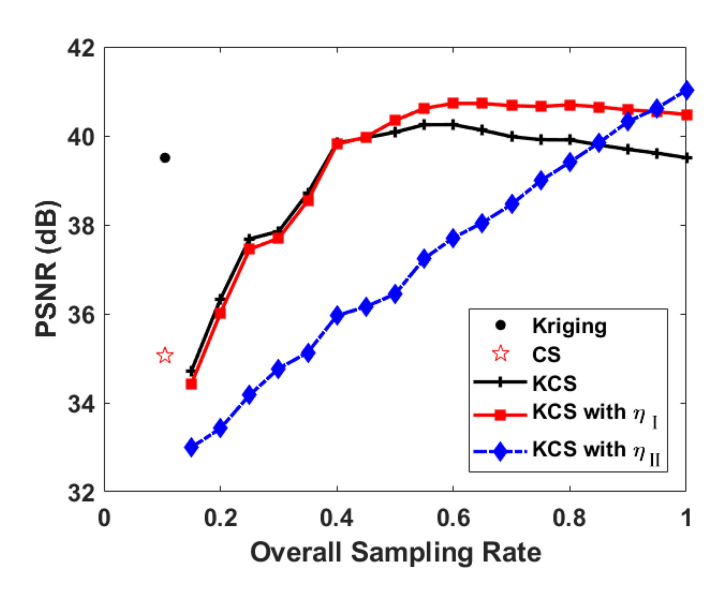


Fig. 9. Reconstruction performance of different methods based on ambient sound level measurements. Single points represent the results for the reconstruction based only on real samples. The lines illustrate the PSNR values over different overall sampling rates.

received signal over a fixed time interval of 2 s. Each calculated acoustic intensity value was associated with a spatial location in the glider's trajectories.

The glider traveled at about 0.25 m/s in the still water. The flow velocity was usually smaller than 1 m/s. The spatial resolution should not be higher than 2.5 m. The dimension of the reconstructed field was  $128 \times 128$ . The sampling rate was 11.66%. Fig. 8(b) shows the reconstructed image by the proposed weighted KCS with  $\eta_{II}$ . The overall sampling rate used was 100%.

Fig. 9 shows the calculated PSNR metric for different methods. The curves represent the performance of the KCS algorithms for different overall sampling rates. Kriging and CS performances were obtained based on real samples. We used the exponential kernel for all the kriging procedures here. Due to the low sampling rate (11.66%) along the kinematically constrained tracks, the performance of the CS-only method was

worst, generating a PSNR of about 35 dB. The kriging method generated a PSNR of 39.5 dB. Three KCS variants, unweighted, weighted with  $\eta_I$ , and weighted with  $\eta_{II}$ , started with a similar performance with the CS-only method when a minimum number of virtual samples were added. When the overall sampling rate increased, up to 60%, the PSNRs of all three variants increased, although at different rates. When the overall sampling rate was 60%, unweighted KCS and KCS with  $\eta_I$  achieved their maximum PSNRs of 40.2 and 40.7 dB, respectively. In contrast, the weighted KCS method with  $\eta_{II}$  showed a monotonic increase in its PSNR as a function of the overall sampling rate. At the overall sampling rate of 100%, it generated a PSNR of 41.1 dB, which was highest among all the reconstruction outcomes.

## B. Reconstruction of Horizontal TL Field

The acoustic TL experiment was conducted at Lake Tuscaloosa, AL, USA, on November 5, 2017. Lake Tuscaloosa is a large reservoir in Tuscaloosa. An acoustic transmission unit, including a transmitter and an amplifier, was installed at a dock near the riverbank. The source sound level was about 187 dB re 1  $\mu$  Pa at 1 m. Chirp signals at the carrier frequency of 85 kHz with a bandwidth of 10 kHz were transmitted in a repeated fashion. The duration of the chirp signal was 50 ms. The silence interval between the chirp transmissions was 200 ms.

The receiving unit was an icListen digital hydrophone installed on the Ecomapper AUV. The sensitivity of the hydrophone was about  $-180\,\mathrm{dB}$  re  $1\,\mathrm{V}/\mu$  Pa. Its frequency response was flat from 10 Hz to 200 kHz. The sampling frequency of the hydrophone was set to 512 kHz. The AUV navigated within the experimental region at a depth of about 3 m.

The recorded acoustic data first passed a bandpass filter with a center frequency of 85 kHz and a bandwidth of 10 kHz. Then, the acoustic intensities were calculated from the filtered measurements by integrating over a complete signal repetition period of 250 ms. The TL values were obtained by subtracting the sound intensity from the sound source level. Each calculated TL value corresponded to a spatial location of the AUV. The spatial resolution of the TL field was restricted by the acoustic intensity

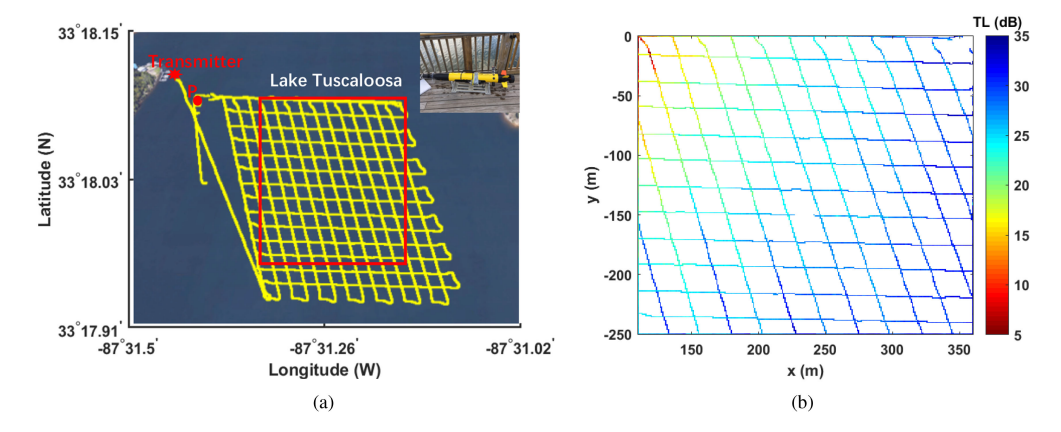


Fig. 10. Acoustic TL experiment conducted with an AUV at Lake Tuscaloosa. (a) AUV trajectories. The acoustic source and AUV parking location are marked as "transmitter" and "P," respectively. A photo of the EcoMapper AUV is also included as an inset. (b) TL measurements within the marked rectangular area in subplot (a).

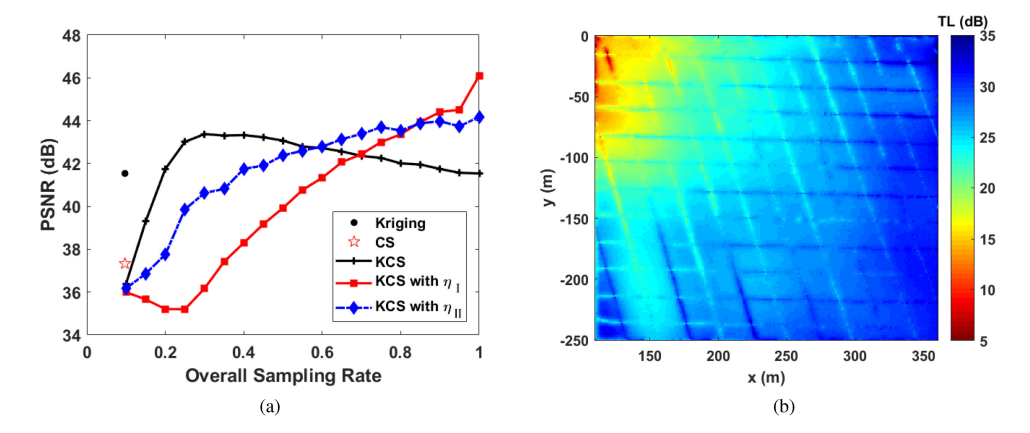


Fig. 11. Acoustic TL field reconstruction. (a) Reconstruction performances of different methods. (b) Reconstructed image by the weighted KCS with  $\eta_I$  at the overall sampling rate of 100%.

integration period and the speed of AUV. During the experiment, the AUV speed was set to 1 m/s. Therefore, the spatial resolution should not be higher than 0.25 m. The discretized dimension of the reconstructed field was  $256\times256$ . Fig. 10(b) shows the TL spatial distribution measurements. The reconstructed field had a spatial resolution of 0.98 m. The sampling rate was 10.79%.

The reconstruction results are presented in Fig. 11. Here, all kriging procedures used the Gaussian kernel. Fig. 11(a) shows the PSNR performance for different reconstruction methods. The results were similar to those in Fig. 9, with larger gains obtained from the KCS methods. The performance of the CSonly method was worst, generating a PSNR of about 37 dB. The kriging method generated a PSNR of 41.5 dB. Three KCS variants, unweighted, weighted with  $\eta_I$ , and weighted with  $\eta_{II}$ , started with a similar performance with the CS-only method when using a minimum number of virtual samples. When the overall sampling rate was about 30%, unweighted KCS method achieved its maximum PSNRs of 43.4 dB. Both weighted KCS methods showed a monotonic increase in their PSNRs when the overall sampling rate increased. At the overall sampling rate of 100%, the weighted KCS method with  $\eta_{II}$  generated a PSNR of 44.2 dB. With the full overall sampling rate, the weighted KCS method with  $\eta_I$  generated a PSNR of 46.1 dB, highest among all the reconstruction outcomes. Fig. 11(b) shows the reconstructed

acoustic TL field from the weighted KCS method with  $\eta_I$  at the full overall sampling rate.

#### VI. CONCLUSION

This article proposed a KCS approach to reconstruct the spatial distribution of underwater acoustic fields based on samples collected along trajectories of underwater vehicles. The key idea of the KCS approach was to introduce virtual samples as inputs to the CS reconstruction. The addition of virtual samples led to a higher probability that the RIP of the sampling matrix was satisfied. Our simulations showed that some performance gains were achieved by using virtual samples in the KCS approach. Such gain was only achieved using a proper amount of virtual samples. When there were too few or too many virtual samples, the reconstruction performance degraded from its optimum. The reason was that the virtual samples come with estimation errors. The advantage of introduced randomness was canceled by the estimation errors in the virtual samples.

To address this issue, we introduced weighting functions to differentiate the virtual samples from the real samples. We analyzed the performance of two weighting functions at different overall sampling rates. Computer simulations demonstrated their advantages over the unweighted KCS method. These two

types of weighting functions had their strengths in different applications and with different kriging kernels. Using the ambient noise measurements from the glider experiment in the South China Sea, the weighted KCS method with  $\eta_{II}$  generated about 2 dB performance gain over the kriging-only method, in terms of the PSNR. In the comparison, both the KCS and kriging-only methods used the exponential kriging kernel. Using the acoustic TL measurements from the AUV experiment, the weighted KCS method with  $\eta_I$  generated about 5 dB gain in the PSNR over the kriging-only method. In this case, both the KCS and kriging-only methods used the Gaussian kernel. Both weighted KCS versions used an overall sampling rate of 100%. In comparison, the unweighted KCS version had smaller PSNR gains over the kriging-only method, about 1–2 dB in both cases, only when a proper amount of virtual samples were used. In both experiments, the real sampling rate was about 11%. The CS-only method did not generate satisfactory results. The CS-only method was about 6 dB worse than the weighted KCS method in the ambient noise reconstruction and about 9 dB worse in the acoustic TL reconstruction, in terms of the PSNR.

## REFERENCES

- H. Matsumoto, J. H. Haxel, R. P. Dziak, D. R. Bohnenstiehl, and R. W. Embley, "Mapping the sound field of an erupting submarine volcano using an acoustic glider," *J. Acoust. Soc. Amer.*, vol. 129, no. 3, pp. EL94–EL99, 2011.
- [2] B. Bingham *et al.*, "Passive and active acoustics using an autonomous wave glider," *J. Field Robot.*, vol. 29, no. 6, pp. 911–923, 2012.
- wave glider," *J. Field Robot.*, vol. 29, no. 6, pp. 911–923, 2012.
  [3] M. Grund, L. Freitag, J. Preisig, and K. Ball, "The PLUSNet underwater communications system: Acoustic telemetry for undersea surveillance," in *Proc. OCEANS Conf.*, 2006, pp. 1–5.
- [4] A. Caiti, V. Calabrò, G. Dini, A. L. Duca, and A. Munafò, "AUVs as mobile nodes in acoustic communication networks: Field experience at the UAN10 experiment," in *Proc. OCEANS Conf.*, 2011, pp. 1–6.
- [5] D. Guihen, S. Fielding, E. J. Murphy, K. J. Heywood, and G. Griffiths, "An assessment of the use of ocean gliders to undertake acoustic measurements of zooplankton: The distribution and density of Antarctic krill (Euphausia superba) in the Weddell Sea," *Limnology Oceanogr., Methods*, vol. 12, no. 6, pp. 373–389, 2014.
- [6] N. S.-N. Lam, "Spatial interpolation methods: A review," Amer. Cartographer, vol. 10, no. 2, pp. 129–150, 1983.
- [7] P. Goovaerts, "Geostatistical approaches for incorporating elevation into the spatial interpolation of rainfall," *J. Hydrol.*, vol. 228, no. 1/2, pp. 113– 129, 2000.
- [8] S. J. Jeffrey, J. O. Carter, K. B. Moodie, and A. R. Beswick, "Using spatial interpolation to construct a comprehensive archive of Australian climate data," *Environ. Model. Softw.*, vol. 16, no. 4, pp. 309–330, 2001.
- [9] M. L. Stein, "Predicting with estimated parameters," in *Interpolation of Spatial Data: Some Theory For Kriging*. New York, NY, USA: Springer, 2012, pp. 160–228.
- [10] Y.-H. Kim, D. A. Shell, C. Ho, and S. Saripalli, "Spatial interpolation for robotic sampling: Uncertainty with two models of variance," in *Experi*mental Robotics. New York, NY, USA: Springer, 2013, pp. 759–774.
- [11] D. Horner, "A data-driven framework for rapid modeling of wireless communication channels," Ph.D. dissertation, Dept. Comput. Sci., Nav. Postgrad. School, Monterey, CA, USA, 2013.
- [12] W. Wu, A. Song, P. Varnell, and F. Zhang, "Cooperatively mapping of the underwater acoustic channel by robot swarms," in *Proc. 9th Int. Conf. Underwater Netw. Syst.*, 2014, pp. 1–8.
- [13] I. Lemmer, "Estimating local recoverable reserves via indicator Kriging," in Geostatistics for natural Resources Characterization. New York, NY, USA: Springer, 1984, pp. 349–364.
- [14] G. Pan, "Restricted Kriging: A link between sample value and sample configuration," *Math. Geol.*, vol. 26, no. 1, pp. 135–155, 1994.
- [15] K. Plengkhom and W. Kanok-Nukulchai, "An enhancement of finite element method with moving Kriging shape functions," *Int. J. Comput. Methods*, vol. 2, no. 4, pp. 451–475, 2005.

- [16] L. M. Brekhovskikh, Y. P. Lysanov, and R. T. Beyer, "Fundamentals of ocean acoustics," *J. Acoust. Soc. Amer.*, vol. 90, no. 6, pp. 3382–3383, 1991
- [17] P. C. Etter, "Acoustical oceanography," in *Underwater Acoustic Modeling and Simulation*. Boca Raton, FL, USA: CRC Press, 2013, pp. 23–60.
- [18] A. D. Waite, "Propagation of sound in the sea," in *Sonar for Practising Engineers*. England, U.K.: Wiley, 2002, pp. 43–66.
- [19] R. Oba and S. Finette, "Acoustic propagation through anisotropic internal wave fields: Transmission loss, cross-range coherence, and horizontal refraction," *J. Acoust. Soc. Amer.*, vol. 111, no. 2, pp. 769–784, 2002.
- [20] M. J. Buckingham, "Theory of the directionality and spatial coherence of wind-driven ambient noise in a deep ocean with attenuation," *J. Acoust. Soc. Amer.*, vol. 134, no. 2, pp. 950–958, 2013.
- [21] Q. Yang, K. Yang, R. Cao, and S. Duan, "Spatial vertical directionality and correlation of low-frequency ambient noise in deep ocean direct-arrival zones," Sensors, vol. 18, no. 2, 2018, Art. no. 319.
- [22] E. J. Candes, J. K. Romberg, and T. Tao, "Stable signal recovery from incomplete and inaccurate measurements," *Commun. Pure Appl. Math.*, vol. LIX, pp. 1207–1223, 2006.
- [23] M. B. Wakin et al., "An architecture for compressive imaging," in Proc. IEEE Int. Conf. Image Process., 2006, pp. 1273–1276.
- [24] J. Sun, A. Song, J. Yu, A. Zhang, and F. Zhang, "Underwater acoustic field reconstruction using a compressive sensing approach," in *Proc. IEEE/MTS OCEANS*, 2017, pp. 1–5.
- [25] M. Rudelson and R. Vershynin, "On sparse reconstruction from Fourier and Gaussian measurements," *Commun. Pure Appl. Math.*, vol. 61, no. 8, pp. 1025–1045, 2008.
- [26] J. P. Haldar, D. Hernando, and Z.-P. Liang, "Compressed-sensing MRI with random encoding," *IEEE Trans. Med. Imag.*, vol. 30, no. 4, pp. 893–903, Apr. 2010.
- [27] J. Romberg, "Compressive sensing by random convolution," SIAM J. Imag. Sci., vol. 2, no. 4, pp. 1098–1128, 2009.
- [28] T. Poggio and T. Vetter, "Recognition and structure from one 2D model view: Observations on prototypes, object classes and symmetries," Massachusetts Inst. Technol., Cambridge, MA, USA, Technical Rep. A. I. Memo 1347, 1992.
- [29] L. Li, Y. Peng, G. Qiu, Z. Sun, and S. Liu, "A survey of virtual sample generation technology for face recognition," *Artif. Intell. Rev.*, vol. 50, no. 1, pp. 1–20, Jun. 2018.
- [30] D.-C. Li and Y.-S. Lin, "Using virtual sample generation to build up management knowledge in the early manufacturing stages," *Eur. J. Oper. Res.*, vol. 175, no. 1, pp. 413–434, 2006.
- [31] P. Niyogi, F. Girosi, and T. Poggio, "Incorporating prior information in machine learning by creating virtual examples," *Proc. IEEE*, vol. 86, no. 11, pp. 2196–2209, Nov. 1998.
- [32] Y. S. Abu-Mostafa, "Hints," *Neural Comput.*, vol. 7, no. 4, pp. 639–671, 1995.
- [33] S. Datta and B. Deka, "Magnetic resonance image reconstruction using fast interpolated compressed sensing," J. Opt., vol. 47, no. 2, pp. 154–165, 2018
- [34] C. Li, C. C. Mosher, and S. T. Kaplan, "Interpolated compressive sensing for seismic data reconstruction," SEG Tech. Program Expanded Abstracts 2012, Soc. Exploration Geophys., Tulsa, OK, USA, 2012, pp. 1–6.
  [35] J. Yu, F. Zhang, A. Zhang, W. Jin, and Y. Tian, "Motion parameter
- [35] J. Yu, F. Zhang, A. Zhang, W. Jin, and Y. Tian, "Motion parameter optimization and sensor scheduling for the Sea-Wing underwater glider," *IEEE J. Ocean. Eng.*, vol. 38, no. 2, pp. 243–254, Apr. 2013.
- [36] U. Mitra et al., "Structured sparse methods for active ocean observation systems with communication constraints," *IEEE Commun. Mag.*, vol. 53, no. 11, pp. 88–96, Nov. 2015.
- [37] R. Hummel, S. Poduri, F. Hover, U. Mitra, and G. Sukhatme, "Mission design for compressive sensing with mobile robots," in *Proc. IEEE Int. Conf. Robot. Autom.*, 2011, pp. 2362–2367.
- [38] F. S. Hover, R. Hummel, U. Mitra, and G. Sukhatme, "One-step-ahead kinematic compressive sensing," in *Proc. IEEE GLOBECOM Workshops*, 2011, pp. 1314–1319.
- [39] B. Chen, P. Pandey, and D. Pompili, "A distributed adaptive sampling soluting using autonomous underwater vehicles," in *Proc. 7th ACM Int. Conf. Underwater Netw. Syst.*, 2012, pp. 1–8.
- [40] S.-J. Kim, E. Dall'Anese, and G. B. Giannakis, "Cooperative spectrum sensing for cognitive radios using Kriged Kalman filtering," *IEEE J. Sel. Topics Signal Process.*, vol. 5, no. 1, pp. 24–36, Feb. 2011.
- [41] J. Sun, J. Yu, A. Zhang, A. Song, and F. Zhang, "Underwater acoustic intensity field reconstruction by Kriged compressive sensing," in *Proc.* 13th ACM Int. Conf. Underwater Netw. Syst., 2018, pp. 1–8.
- [42] V. Blobel, "Unfolding methods in particle physics," in *Proc. PHYSTAT* 2011 Workshop Statist. Issues Related Discovery Claims Search Exp. Unfolding, 2011, pp. 240–251.

- [43] S. Mallat, "Wavelet zoom," in A Wavelet Tour of Signal Processing, Third Edition: The Sparse Way. Orlando, FL, USA: Academic, 2008, pp. 205–259.
- [44] M. N. Do and M. Vetterli, "The contourlet transform: An efficient directional multiresolution image representation," *IEEE Trans. Image Process.*, vol. 14, no. 12, pp. 2091–2106, Dec. 2005.
- [45] D. L. Donoho, "Compressed sensing," *IEEE Trans. Inf. Theory*, vol. 52, no. 4, pp. 1289–1306, Apr. 2006.
- [46] E. J. Candès, J. Romberg, and T. Tao, "Robust uncertainty principles: Exact signal reconstruction from highly incomplete frequency information," *IEEE Trans. Inf. Theory*, vol. 52, no. 2, pp. 489–509, Feb. 2006.
- [47] M. Bertero and P. Boccacci, "Iterative regularization methods," in *Introduction to Inverse Problems in Imaging*. London, U.K.: CRC Press, 1998, pp. 137–167.
- [48] T. Blumensath and M. E. Davies, "Iterative thresholding for sparse approximations," *J. Fourier Anal. Appl.*, vol. 14, no. 5/6, pp. 629–654, 2008
- [49] J. E. Fowler, S. Mun, and E. W. Tramel, "Block-based compressed sensing of images and video," *Found. Trends Signal Process.*, vol. 4, no. 4, pp. 297– 416, 2012.
- [50] L. Gan, "Block compressed sensing of natural images," in *Proc. 15th Int. Conf. Digit. Signal Process.*, 2007, pp. 403–406.
- [51] Q. Huynh-Thu and M. Ghanbari, "Scope of validity of PSNR in image/video quality assessment," *Electron. Lett.*, vol. 44, no. 13, pp. 800–801, 2008.
- [52] Z. Wang, A. C. Bovik, H. R. Sheikh, and E. P. Simoncelli, "Image quality assessment: From error visibility to structural similarity," *IEEE Trans. Image Process.*, vol. 13, no. 4, pp. 600–612, Apr. 2004.
- [53] N. Cressie, "Statistics for spatial data," Terra Nova, vol. 4, no. 5, pp. 613–617, 1992.
- [54] J. M. Duarte-Carvajalino and G. Sapiro, "Learning to sense sparse signals: Simultaneous sensing matrix and sparsifying dictionary optimization," *IEEE Trans. Image Process.*, vol. 18, no. 7, pp. 1395–1408, Jul. 2009.
- [55] H. Lee, H. Oh, S. Lee, and A. C. Bovik, "Visually weighted compressive sensing: Measurement and reconstruction," *IEEE Trans. Image Process.*, vol. 22, no. 4, pp. 1444–1455, Apr. 2013.
- [56] H. Lee and S. Lee, "Visual entropy gain for wavelet image coding," *IEEE Signal Process. Lett.*, vol. 13, no. 9, pp. 553–556, Sep. 2006.
- [57] NOAA National Centers for Environmental Information, "ETOPO1 global relief model," Mar. 1, 2009. [Online]. Available: https://ngdc.noaa.gov/ mgg/global/global.htm, Accessed on: Jan. 10, 2018.
- [58] South China Sea Institute of Oceanology, "A new-generation real-time forecasting system for the South-China-Sea marine environment," Jun. 2011. [Online]. Available: http://210.77.90.43/new/, Accessed on: Aug. 1, 2018.
- [59] Heat, Light, and Sound Research, Inc., "Acoustics toolbox," Jul. 25, 2016.
  [Online]. Available: http://oalib.hlsresearch.com/AcousticsToolbox/, Accessed on: Mar. 10, 2019.



**Jie Sun** (Member, IEEE) received the B.S. degree in marine technology and the M.S. degree in acoustics from the Ocean University of China, Qingdao, China, in 2011 and 2014, respectively. She is currently working toward the Ph.D. degree in mechatronic engineering with Shenyang Institute of Automation, Chinese Academy of Sciences, Shenyang, China.

She is also a Research Assistant with Shenyang Institute of Automation, Chinese Academy of Sciences. Her research interests include acoustic applications and technology for underwater vehicles and mobile sensor networks.



Shijie Liu (Member, IEEE) received the B.S. degree in electrical and information engineering from Anhui Normal University, Wuhu, China, in 2012, and the Ph.D. degree in mechatronic engineering from Shenyang Institute of Automation, Chinese Academy of Sciences, Shenyang, China, in 2019.

His research interests include mobile sensing and marine autonomy.

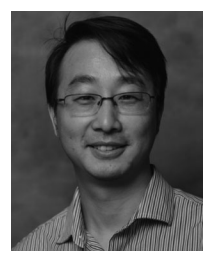


Fumin Zhang (Senior Member, IEEE) received the B.S. and M.S. degrees in electrical engineering from Tsinghua University, Beijing, China, in 1995 and 1998, respectively, and the Ph.D. degree in electrical and computer engineering from the University of Maryland, College Park, MD, USA, in 2004.

In 2007, he joined the School of Electrical and Computer Engineering, Georgia Institute of Technology, Atlanta, GA, USA, where he is currently a Professor. From 2004 to 2007, he was a Lecturer and a Postdoctoral Research Associate with the Mechanical

and Aerospace Engineering Department, Princeton University, Princeton, NJ, USA. His research interests include marine autonomy, mobile sensor networks, and theoretical foundations for battery-supported cyber-physical systems.

Dr. Zhang received the National Science Foundation CAREER Award in 2009 and the Office of Naval Research Young Investigator Program Award in 2010.



**Aijun Song** (Member, IEEE) received the Ph.D. degree in electrical engineering from the University of Delaware, Newark, DE, USA, in 2005.

He is currently an Assistant Professor with the Department of Electrical and Computer Engineering, University of Alabama, Tuscaloosa, AL, USA. From 2005 to 2008, he was a Postdoctoral Research Associate with the College of Earth, Ocean and Environment, University of Delaware. During this period, he was also an Office of Naval Research (ONR) Postdoctoral Fellow, supported by the special research

award in the ONR Ocean Acoustics program. He was an Assistant Research Professor with the University of Delaware from 2008 to 2014 and an Associate Research Professor from 2014 to 2015. His current research interests include digital communications and signal processing techniques for radio frequency and underwater acoustic channels, ocean acoustics, sensor networks, and ocean monitoring and exploration.

Dr. Song was the General Co-Chair of the 2018 March NSF Workshop on Underwater Wireless Communications and Networking and the 2018 November NSF Workshop on Underwater Wireless Infrastructure. He was the General Co-Chair of the 14th International Conference on Underwater Networks & Systems.



Jiancheng Yu received the B.S. degree in mechanical engineering and the M.S. degree in mechanical design and theory from Northeastern University, Shenyang, China, in 2000 and 2003, respectively, and the Ph.D. degree in mechatronic engineering from Shenyang Institute of Automation, Chinese Academy of Sciences, Shenyang, in 2006.

He is currently a Professor with Shenyang Institute of Automation. His research interests include control theory and method research for underwater vehicles and new concepts of underwater vehicle design.



**Aiqun Zhang** received the B.S. degree in mechanical engineering from Northeastern University, Shenyang, China, in 1982.

He spent more than 30 years developing underwater vehicles, first as the Director of the Marine Robotics Department, Shenyang Institute of Automation, Chinese Academy of Sciences, Shenyang, and more recently as the Engineer-in-Chief with the Institute of Deep-Sea Science and Engineering, Chinese Academy of Sciences, Sanya, China. His research interests include overall design for underwater vehicles

and technologies for extreme deep-sea exploration.